

PUBLISHED VERSION

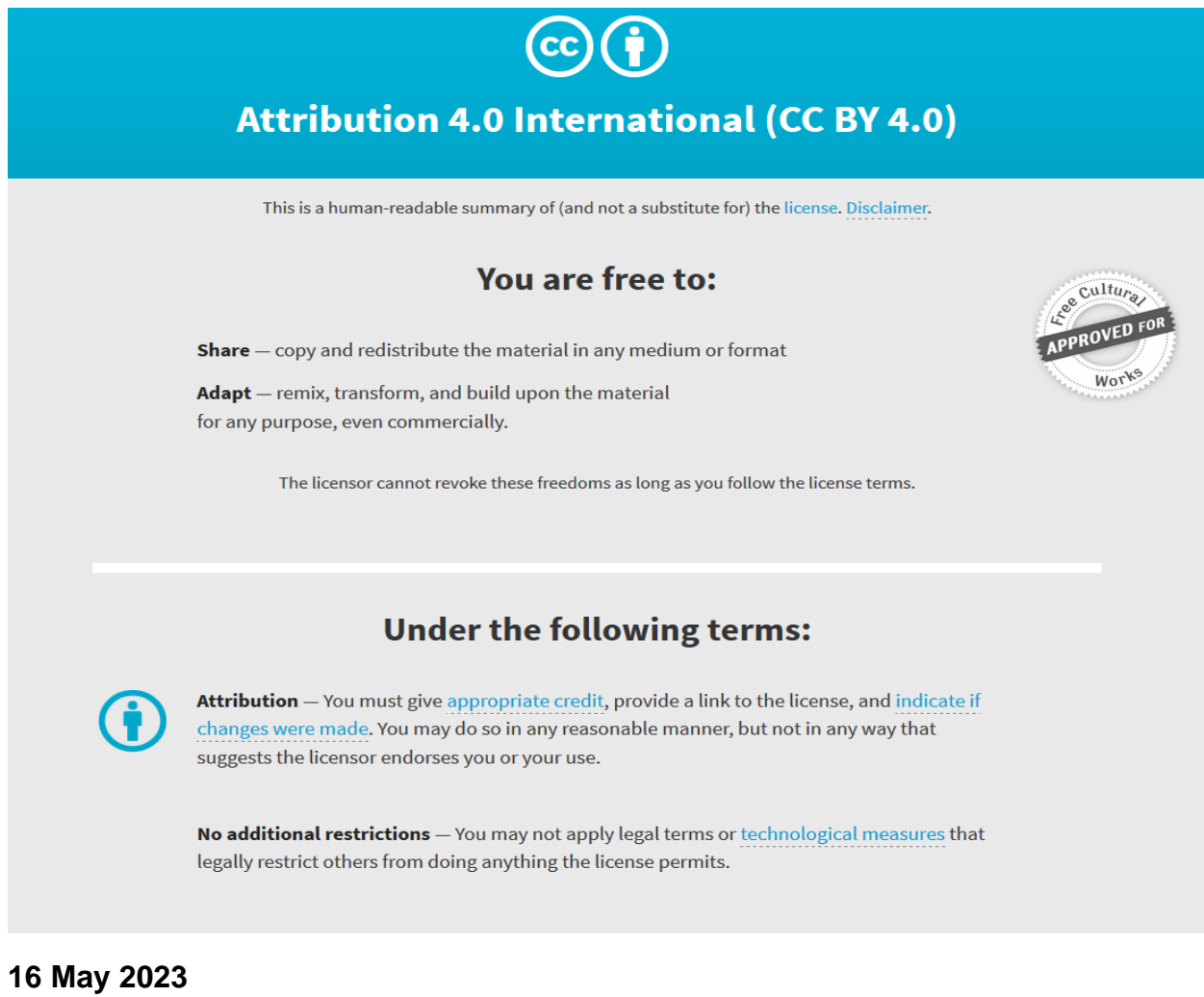
Wenguo Zhu, Niko Eckerskorn, Avinash Upadhyaya, Li Li, Andrei V. Rode, and Woei Ming Lee
Dynamic axial control over optically levitating particles in air with an electrically-tunable variable-focus lens
Biomedical Optics Express, 2016; 7(7):2902-2911

©2016 Optical Society of America. Open Access (CC BY 4.0)

Published version <http://dx.doi.org/10.1364/BOE.7.002902>

PERMISSIONS

<http://creativecommons.org/licenses/by/4.0/>



The image shows a Creative Commons Attribution 4.0 International License (CC BY 4.0) graphic. It features a blue header with the CC logo and a person icon, followed by the text "Attribution 4.0 International (CC BY 4.0)". Below this, there is a disclaimer: "This is a human-readable summary of (and not a substitute for) the license. [Disclaimer.](#)". The main body is divided into two sections: "You are free to:" and "Under the following terms:". Under "You are free to:", there are two bullet points: "Share — copy and redistribute the material in any medium or format" and "Adapt — remix, transform, and build upon the material for any purpose, even commercially.". Below these is a note: "The licensor cannot revoke these freedoms as long as you follow the license terms.". Under "Under the following terms:", there are two bullet points: "Attribution — You must give [appropriate credit](#), provide a link to the license, and [indicate if changes were made](#). You may do so in any reasonable manner, but not in any way that suggests the licensor endorses you or your use." and "No additional restrictions — You may not apply legal terms or [technological measures](#) that legally restrict others from doing anything the license permits.". On the right side of the graphic, there is a circular seal that says "Free Cultural Works APPROVED FOR". At the bottom left, the date "16 May 2023" is displayed.

Attribution 4.0 International (CC BY 4.0)

This is a human-readable summary of (and not a substitute for) the [license](#). [Disclaimer.](#)

You are free to:

- Share** — copy and redistribute the material in any medium or format
- Adapt** — remix, transform, and build upon the material for any purpose, even commercially.

The licensor cannot revoke these freedoms as long as you follow the license terms.

Under the following terms:

- Attribution** — You must give [appropriate credit](#), provide a link to the license, and [indicate if changes were made](#). You may do so in any reasonable manner, but not in any way that suggests the licensor endorses you or your use.
- No additional restrictions** — You may not apply legal terms or [technological measures](#) that legally restrict others from doing anything the license permits.

16 May 2023

<https://hdl.handle.net/2440/138396>

Dynamic axial control over optically levitating particles in air with an electrically-tunable variable-focus lens

WENGUO ZHU,^{1,2,4} NIKO ECKERSKORN,¹ AVINASH UPADHYA,³ LI LI,^{1,2}
ANDREI V. RODE,^{1,5} AND WOEI MING LEE^{3,4,6}

¹Laser Physics Centre, Research School of Physics and Engineering, The Australian National University, Canberra, ACT 2601, Australia

²The State Key Laboratory of Optoelectronic Materials and Technologies, Sun Yat-sen University, Guangzhou 510275, China

³Research School of Engineering, The Australian National University, Canberra ACT 0200, Australia

⁴Equal contribution

⁵andrei.ode@anu.edu.au

⁶steve.lee@anu.edu.au

Abstract: Efficient delivery of viruses, proteins and biological macromolecules into a micrometer-sized focal spot of an XFEL beam for coherent diffraction imaging inspired new development in touch-free particle injection methods in gaseous and vacuum environments. This paper lays out our ongoing effort in constructing an all-optical particle delivery approach that uses piconewton photophoretic and femtonewton light-pressure forces to control particle delivery into the XFEL beam. We combine a spatial light modulator (SLM) and an electrically tunable lens (ETL) to construct a variable-divergence vortex beam providing dynamic and stable positioning of levitated micrometer-size particles, under normal atmospheric pressure. A sensorless wavefront correction approach is used to reduce optical aberrations to generate a high quality vortex beam for particle manipulation. As a proof of concept, stable manipulation of optically-controlled axial motion of trapped particles is demonstrated with a response time of 100ms. In addition, modulation of trapping intensity provides a measure of the mass of a single, isolated particle. The driving signal of this oscillatory motion can potentially be phase-locked to an external timing signal enabling synchronization of particle delivery into the x-ray focus with XFEL pulse train.

©2016 Optical Society of America

OCIS codes: (140.7010) Laser trapping; (350.4855) Optical tweezers or optical manipulation.

References and links

1. H. N. Chapman, A. Barty, M. J. Bogan, S. Boutet, M. Frank, S. P. Hau-Riege, S. Marchesini, B. W. Woods, S. Bajt, W. H. Benner, R. A. London, E. Plonjes, M. Kuhlmann, R. Treusch, S. Dusterer, T. Tschentscher, J. R. Schneider, E. Spiller, T. Moller, C. Bostedt, M. Hoener, D. A. Shapiro, K. O. Hodgson, D. van der Spoel, F. Burmeister, M. Bergh, C. Caleman, G. Huldt, M. M. Seibert, F. R. N. C. Maia, R. W. Lee, A. Szoke, N. Timneanu, and J. Hajdu, "Femtosecond diffractive imaging with a soft-X-ray free-electron laser," *Nat. Phys.* **2**(12), 839–843 (2006).
2. V. Marx, "Structural biology: 'seeing' crystals the XFEL way," *Nat. Methods* **11**(9), 903–908 (2014).
3. D. P. DePonte, U. Weierstall, K. Schmidt, J. Warner, D. Starodub, J. C. H. Spence, and R. B. Doak, "Gas dynamic virtual nozzle for generation of microscopic droplet streams," *J. Phys. D Appl. Phys.* **41**(19), 195505 (2008).
4. M. J. Bogan, W. H. Benner, S. Boutet, U. Rohner, M. Frank, A. Barty, M. M. Seibert, F. Maia, S. Marchesini, S. Bajt, B. Woods, V. Riot, S. P. Hau-Riege, M. Svenda, E. Marklund, E. Spiller, J. Hajdu, and H. N. Chapman, "Single particle X-ray diffractive imaging," *Nano Lett.* **8**(1), 310–316 (2008).
5. J. Küpper, S. Stern, L. Holmegaard, F. Filsinger, A. Rouzée, A. Rudenko, P. Johnsson, A. V. Martin, M. Adolph, A. Aquila, S. Bajt, A. Barty, C. Bostedt, J. Bozek, C. Caleman, R. Coffee, N. Coppola, T. Delmas, S. Epp, B. Erk, L. Foucar, T. Gorkhover, L. Gumprecht, A. Hartmann, R. Hartmann, G. Hauser, P. Holl, A. Hömke, N. Kimmel, F. Krasniqi, K.-U. Kühnel, J. Maurer, M. Messerschmidt, R. Moshhammer, C. Reich, B. Rudek, R. Santra, I. Schlichting, C. Schmidt, S. Schorb, J. Schulz, H. Soltau, J. C. H. Spence, D. Starodub, L. Strüder, J. Thøgersen, M. J. J. Vrakking, G. Weidenspointner, T. A. White, C. Wunderer, G. Meijer, J. Ullrich, H. Stapelfeldt, D. Rolles, and H. N. Chapman, "X-Ray Diffraction from Isolated and Strongly Aligned Gas-Phase Molecules with a Free-Electron Laser," *Phys. Rev. Lett.* **112**(8), 083002 (2014).

6. U. Weierstall, D. James, C. Wang, T. A. White, D. Wang, W. Liu, J. C. H. Spence, R. Bruce Doak, G. Nelson, P. Fromme, R. Fromme, I. Grotjohann, C. Kupitz, N. A. Zatsepin, H. Liu, S. Basu, D. Wacker, G. W. Han, V. Katritch, S. Boutet, M. Messerschmidt, G. J. Williams, J. E. Koglin, M. Marvin Seibert, M. Klinker, C. Gati, R. L. Shoeman, A. Barty, H. N. Chapman, R. A. Kirian, K. R. Beyerlein, R. C. Stevens, D. Li, S. T. A. Shah, N. Howe, M. Caffrey, and V. Cherezov, "Lipidic cubic phase injector facilitates membrane protein serial femtosecond crystallography," *Nat. Commun.* **5**, 3309 (2014).
7. V. G. Shvedov, A. S. Desyatnikov, A. V. Rode, W. Krolikowski, and Y. S. Kivshar, "Optical guiding of absorbing nanoclusters in air," *Opt. Express* **17**(7), 5743–5757 (2009).
8. A. S. Desyatnikov, V. G. Shvedov, A. V. Rode, W. Krolikowski, and Y. S. Kivshar, "Photophoretic manipulation of absorbing aerosol particles with vortex beams: theory versus experiment," *Opt. Express* **17**(10), 8201–8211 (2009).
9. V. G. Shvedov, A. V. Rode, Y. V. Izdebskaya, A. S. Desyatnikov, W. Krolikowski, and Y. S. Kivshar, "Giant optical manipulation," *Phys. Rev. Lett.* **105**(11), 118103 (2010).
10. B. Redding, S. C. Hill, D. Alexson, C. Wang, and Y.-L. Pan, "Photophoretic trapping of airborne particles using ultraviolet illumination," *Opt. Express* **23**(3), 3630–3639 (2015).
11. N. W. Shi Kam, T. C. Jessop, P. A. Wender, and H. Dai, "Nanotube Molecular Transporters: Internalization of Carbon Nanotube-Protein Conjugates into Mammalian Cells," *J. Am. Chem. Soc.* **126**(22), 6850–6851 (2004).
12. N. Eckerskorn, R. Bowman, R. A. Kirian, S. Awel, M. Wiedorn, J. Küpper, M. J. Padgett, H. N. Chapman, and A. V. Rode, "Optically Induced Forces Imposed in an Optical Funnel on a Stream of Particles in Air or Vacuum," *Phys. Rev. Appl.* **4**(6), 064001 (2015).
13. N. Eckerskorn, L. Li, R. A. Kirian, J. Küpper, D. P. DePonte, W. Krolikowski, W. M. Lee, H. N. Chapman, and A. V. Rode, "Hollow Bessel-like beam as an optical guide for a stream of microscopic particles," *Opt. Express* **21**(25), 30492–30499 (2013).
14. H. N. Chapman, P. Fromme, A. Barty, T. A. White, R. A. Kirian, A. Aquila, M. S. Hunter, J. Schulz, D. P. DePonte, U. Weierstall, R. B. Doak, F. R. N. C. Maia, A. V. Martin, I. Schlichting, L. Lomb, N. Coppola, R. L. Shoeman, S. W. Epp, R. Hartmann, D. Rolles, A. Rudenko, L. Foucar, N. Kimmel, G. Weidenspointner, P. Holl, M. Liang, M. Barthelmeß, C. Caleman, S. Boutet, M. J. Bogan, J. Krzywinski, C. Bostedt, S. Bajt, L. Gumprecht, B. Rudek, B. Erk, C. Schmidt, A. Hömke, C. Reich, D. Pietschner, L. Strüder, G. Hauser, H. Gorke, J. Ullrich, S. Herrmann, G. Schaller, F. Schopper, H. Soltau, K.-U. Kühnel, M. Messerschmidt, J. D. Bozek, S. P. Hau-Riege, M. Frank, C. Y. Hampton, R. G. Sierra, D. Starodub, G. J. Williams, J. Hajdu, N. Timneanu, M. M. Seibert, J. Andreasson, A. Røcker, O. Jönsson, M. Svenda, S. Stern, K. Nass, R. Andritschke, C.-D. Schröter, F. Krasniqi, M. Bott, K. E. Schmidt, X. Wang, I. Grotjohann, J. M. Holton, T. R. M. Barends, R. Neutze, S. Marchesini, R. Fromme, S. Schorb, D. Rupp, M. Adolph, T. Gorkhover, I. Andersson, H. Hirsemann, G. Potdevin, H. Graafsma, B. Nilsson, and J. C. H. Spence, "Femtosecond X-ray protein nanocrystallography," *Nature* **470**(7332), 73–77 (2011).
15. B. F. Grewe, F. F. Voigt, M. van 't Hoff, and F. Helmchen, "Fast two-layer two-photon imaging of neuronal cell populations using an electrically tunable lens," *Biomed. Opt. Express* **2**(7), 2035–2046 (2011).
16. A. Jesacher, A. Schwaighofer, S. Fürhapter, C. Maurer, S. Bernet, and M. Ritsch-Marte, "Wavefront correction of spatial light modulators using an optical vortex image," *Opt. Express* **15**(9), 5801–5808 (2007).
17. L. Rkhouak, M. J. Tang, J. C. J. Camp, J. McGregor, I. M. Watson, R. A. Cox, M. Kalberer, A. D. Ward, and F. D. Pope, "Optical trapping and Raman spectroscopy of solid particles," *Phys. Chem. Chem. Phys.* **16**(23), 11426–11434 (2014).

1. Introduction

X-ray free-electron lasers (XFELs), operating at wavelengths of a few nanometers and pulse lengths of ~50 fs, focused down to a few micrometer (0.1 μm – 5 μm) offer near-atomic resolutions in structural imaging of nanometer- to micrometer-sized objects such as membrane proteins and viruses that are very complex, and difficult or impossible to crystallise for conventional X-ray crystallography [1]. The focal region of the XFEL beam presents a window to observe structural evolution of chemical processes with atomic level resolution [2] *in situ* and draws new understanding of biological proteins. XFELs imaging permits imaging macromolecules that do not need to be crystallised or are difficult to crystallize. Particle delivery instruments in an XFEL imaging system need to be capable of introducing contamination-free, uncharged, mono-dispersed, with high density and micrometer-scale positional precision. The delivery process is further complicated by the challenge of retaining the structure of delicate proteins, especially membrane proteins, which becomes highly unstable after removal from their natural membrane environment. Common techniques used to deliver particles include liquid jets formed by gas dynamic virtual nozzles [3], aerodynamic aerosol focusing [4], gas-phase supersonic jet/molecular beam injectors [5] and more recently lipidic cubic phase (LCP) extrusion injectors [6]. In the case of aerosol injection, XFEL experiments are overly time consuming and inefficient, which is especially important for precious samples that cannot be produced in high abundance. A precise touch-

free particle manipulation technique is desired for high-throughput particle delivery solution. Apart from particle delivery, XFEL imaging relies on the quality of the diffraction patterns from non-crystalline and nano-crystalline parts of the particle in order to determine structures *ab initio*. Liquid jet injectors are ideal in that they introduce biomolecules in physiological conditions, but unfortunately they produce background scatter that can severely limit resolution in the case of single-particle imaging. Ideally, non-crystalline particles would be introduced in the gas phase, with only a few monolayers of solvent surrounding each particle to ensure structures of physiological relevance but with minimal solvent scatter.

Three dimensional optical manipulation of solid micro-particles in gas and vacuum presents a new means to interrogate its environment and control the delivery of particles to the XFEL imaging beam. Optical trapping of light-absorbing particles in a gaseous environment is largely influenced by laser-induced photophoretic force [7, 8]. Photophoretic forces originate from the anisotropic heating of surrounding gas molecules that is controlled by the mean free path of the gas molecules, absorption coefficient and thermal conductivity. The photophoretic forces can be orders of magnitude stronger than the force of radiation pressure induced by the same light intensity. Photophoresis in gas environment provides the ability to manipulate absorptive microparticles over macroscopic distance (up to meters [9]) with micrometer precision. Absorptive single walled carbon nanotubes, which could be trapped with photophoretic force [10], have been shown to be able to encapsulate molecular proteins [11].

Our experiments are built upon a concept of trapping and guiding particles in gas media with a sculptured laser beam, referred to as an “optical pipeline” [9, 12, 13]. With both photophoretic forces and light pressure forces, the momentum transfer acts in the direction away from the region of higher optical intensity. For this reason, the beam structures needed for trapping light-absorbing particles need to have a minimum intensity on the beam axis, such as vortex beam or first-order Bessel beams. The sculptured beam with an annular ring intensity forms high-aspect-ratio optical microchannels that are dynamically tuned to control particle delivery in medium- to low-vacuum regimes ($> 10^{-5}$ mbar). We recently mapped the optically induced force to the intensity distribution in the trap in air and under various gas pressures in the range from 5 mbar to 2 bar [12]. The next step in our work is to provide additional time-controlled positioning of particles by changing the divergence of an optical vortex beam. Dynamic control over the beam divergence makes it possible to synchronize the arrival of particles to the focus volume of the X-ray pulses with the train of X-ray pulses from XFEL. Using a spatial light modulator (SLM) and a commercially available electrically tunable lens (ETL), we demonstrate that a single particle can be remotely positioned at accuracy of ~ 1 μm and with a response time of around 100 ms. The particles are shown to change physical position in accordance with the different waveforms (sinusoidal and square) driving the axial position of the focus. These results suggest the possibility of phase-locking a particle that is optically trapped in a structured beam with an external timing signal such as XFEL where the repetition rates is about 100 Hz [14]. The combination of a SLM and ETL provided new capabilities to rapidly control the position of optically trapped particles and synchronise their delivery to the X-ray focal volume with the emission of the X-ray pulses.

2. Method

In order to demonstrate and characterize particle response to the changes of the trapping beam parameters, we built up an experimental setup which consists of three major parts, namely, a particle trapping chamber, an orthogonal microscope imaging platform for characterization of the particle (CCD1, MO2) and a beam characterization system (CCD2, MO3). The annular ring laser beam is focused with a variable-focus optical system and directed upward into the trapping chamber. The particles are trapped and levitate along the axis of the diverging vortex beam where the optically induced forces are counter-balanced by the gravitational force. The equilibrium position can be changed by modulating the laser beam intensity or beam divergence and depends on the particle size, mass and drag force. Here, the beam divergence is changed with a variable focus lens that then alters the equilibrium position of the particle.

The particle response is characterized using a microscope lens that images the particle onto a fast imaging camera. We used solid graphite spheres with a diameter in the range $2\ \mu\text{m}$ to $12\ \mu\text{m}$ (Sigma Aldrich #484164) with known reflectivity and absorption in these experiments.

2.1. Experimental setup

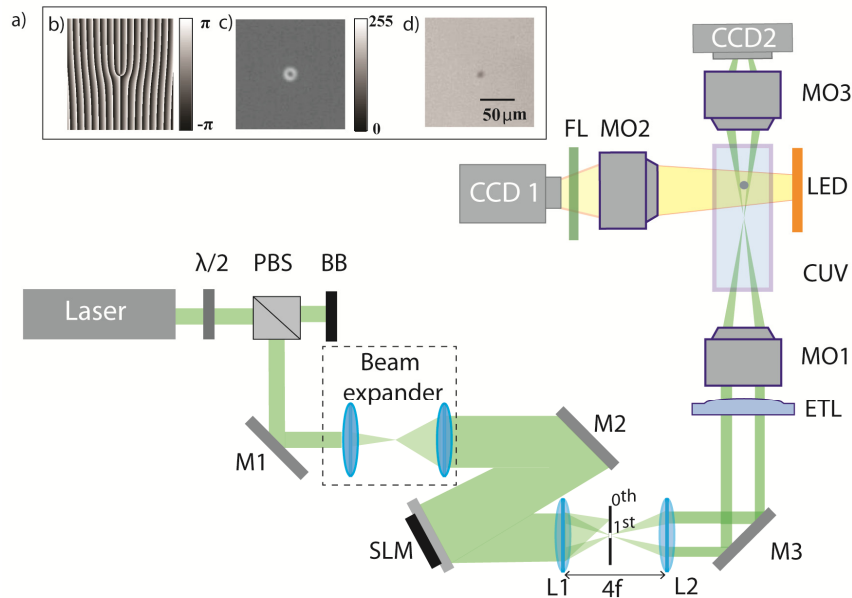


Fig. 1. Schematic representation of the experimental setup. A $532\ \text{nm}$ *cw* laser beam is expanded and directed onto a spatial light modulator (SLM). A blazed grating is added to the SLM-generated optical vortex to select and spatially filter by a circular aperture the first diffraction order. The vortex beam is further projected onto the back focal plane of the microscope objective (MO1) after passing through the electrically tunable lens (ETL). Particle dynamics within a glass cuvette (CUV) is captured by CCD1 via imaging microscope objective (MO2), FL is a notch filter. Beam characterisation is carried out by CCD2 and 3rd microscope objective (MO3). b) – The off-axis hologram used to create the optical vortex beam; c) – image of the optical vortex beam in CCD2 after compensating for aberrations; d) – image of an optically levitated particle in CCD1.

The experimental setup is presented schematically in Fig. 1. A $532\ \text{nm}$ continuous wave (*cw*) laser beam directed is onto a half waveplate followed by a polarising beam splitter cube, which acts as a variable power attenuator. The beam is then redirected onto a beam expander followed by a reflective phase-only spatial light modulator with 1920×1080 pixels of $8\ \mu\text{m}$ pitch (Holoeye Pluto-VIs). A blazed grating is added to the original vortex phase in the spatial light modulator in order to diffract the desired beam efficiently to the first order, which is spatially filtered with a circular aperture placed between two lenses ($L1 = L2 = 500\ \text{mm}$). After passing through the electrical tunable lens (ETL, Optotune EL-10-30-C), the collimated beam is focused by a $10\times$ microscope objective (MO1) with working distance $33.5\ \text{mm}$ and $NA = 0.25$, and forms a diverging vortex beam after focus. The diverging part of the beam is deployed to trap light-absorbing particles, dropped from the top into the glass cuvette (CUV). The trapped particles are imaged by a combination of a $4\times$ objective (MO2) and a notch filter (FL), and a fast camera (Genie HM640). The notch filter is used to block the laser light scattered from the particles so that the trapped particles are imaged on CCD1 using microscope objective MO2. A second camera (CCD2) with a microscope objective (MO3) are positioned along the propagation direction of the beam during beam characterisation. An optical fibre based aberration correction method in-conjunction with the spatial light modulator is setup to retrieve the aberrations in the optical system as described in section 2.2.

The tunable lens consists of a flexible spherical membrane with a radius that changes with voice-coil activated pressure exerted on its outer zone. The tunable lens can provide rapid changes in focal length of up to 1 kHz using an external current driver. These commercial electrically tunable lenses were used in high speed volumetric imaging for two photon microscopy [15] because it can rapidly change beam focus along its axial direction by controlling the divergence of the beam at the back aperture of the microscope objective. The amplitude of the focal length change is proportional to the applied current (mA). In section 2.3, we present the characteristic of a divergent vortex beam with axially variable focus position controlled by the tunable lens.

2.2. Fiber based aberration correction

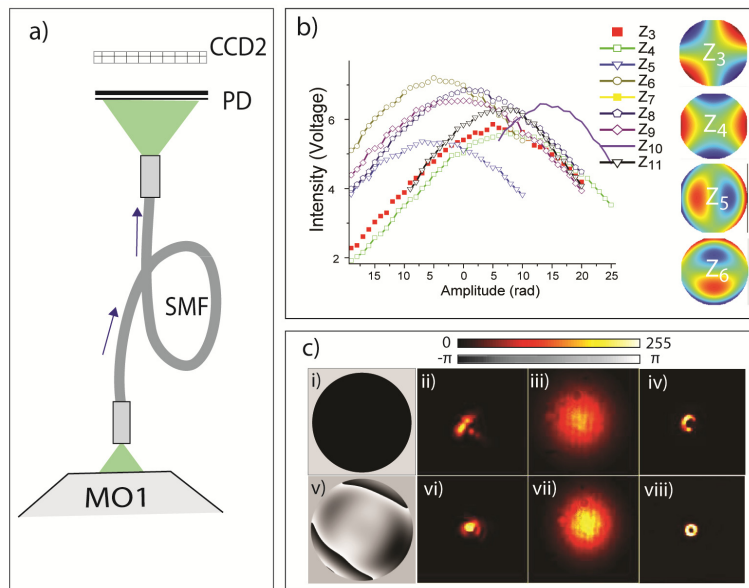


Fig. 2. Sensorless wavefront correction technique with single mode fibre. a) the focus beam is launched into a single mode fibre that relays the beam intensity onto the photodiode (PD) which records the intensity after each Zernike mode. A second charged coupled device (CCD2) verifies the increase intensity at fibre output before and after compensation. b) shows the varying intensity voltage over different Zernike amplitude (inset show example of zernike from Z_3 to Z_6). c) (i) without correcting mask, (ii) intensity at objective lens output before compensation, (iii) output intensity of fibre, (iv) aberrated optical vortex, (v) retrieve mask, (vi) intensity at the objective lens output, (vii) intensity of beam intensity output, (viii) intensity of optical vortex beam after imposing the mask.

Stable lateral confinement of the particle on-axis required an even intensity distribution and minimal aberrations. Optical vortices are generated using a helical 2π phase shift and are known to be easily distorted by optical aberrations [16]. To optimize the beam quality, we set up a fibre based aberration correction method to retrieve the aberrations in the optical system. The approach relies on the confocality of the setup, after adjusting for tip, tilt, and focus, as shown in Fig. 2. For this approach to work, the single mode field diameter of the optical fibre is approximately the size of the beam radius at $1/e^2$ of the intensity. With that assumption, the optical fibre acts like a pinhole optimised for transmitting the maximum intensity of a well-defined input Gaussian mode with a fixed diameter. Hence any beam deviating from the ideal Gaussian will result in weak transmission. The optical vortex mask was first replaced with flat wavefront at the SLM to generate a Gaussian beam. Then a single mode fibre is laced at the focus of the objective (MO1, NA = 0.25) to maximise the laser input that is measured by the photodiode (PD) placed at the fibre output. The size of fibre (mode-field diameter 3.6 - 5.3 μm , Thorlabs P1-630A-FC-1) should be close to that of the beam waist at the focus. The

intensity of light emitted from the fibre is measured in terms of voltage by an amplified silicon photodetector (Thorlabs, PDA100A-EC), as shown in Fig. 2(a). Using this configuration, the intensity at the fibre output is maximised iteratively for each of the first 11 Zernike modes on the SLM. Some of the examples of Zernike modes of astigmatism (Z_3, Z_4) and coma (Z_5, Z_6) are shown in Fig. 2(b). A closed-loop routine was run to maximise the intensity at the fibre output. The Zernike mode $a_i Z_i$ is introduced into the wavefront by the SLM. The power of the output power from the fiber is then monitored by the photodetector. The SLM imposes a range of amplitude on each Zernike mode a_i from -10π radians to 10π radians with 0.4π each step that modulates the coupling beam. As plotted in Fig. 2(b), the measured intensity curves are acquired for each Zernike mode Z_i with the appropriate amplitude a_i for each mode used to maximize the output intensity. Due to the orthogonality of Zernike modes over a unit circle, the optimum correction hologram can be obtained by simply combining the weighed Zernike modes, $Z_{Total} \approx \sum_{i=1}^{11} a_i Z_i$. After correcting for the beam, the

laser intensity at the fibre output is increased by around 30%. The variation of the intensity is plotted against each Zernike amplitude and fitted to a Gaussian curve. Each coefficient of the Zernike amplitude corresponding to the maximum intensity is retrieved and added to the compensation mask Z_{total} . The beam spots at the fiber input and output are shown in Fig. 2(c). Without any correction mask Fig. 2(c i), the beam spot is visibly distorted Fig. 2(c ii) with low output intensity Fig. 2(ciii). This is reflected in a non-uniformed optical vortex beam in Fig. 2(civ). Based on the iteration process, a correction mask is applied, Fig. 2(cv) that generates a beam spot at the input of the fiber resembling a well-defined Airy disc as shown in Fig. 2(cvi) with a higher output intensity and smooth annular intensity, Fig. 2(cvii).

2.3. Characterization of diverging vortex beam

Electrically tunable lenses (ETL) are composed of a thin interface transparent membrane (optical elastomer) that encloses a high refractive index liquid in a chamber. A voice coil actuator exerts pressure around the chamber that forces fluid into the centre of the lens causing a change in lens curvature at repetition rates of up to ~ 1 kHz. To ensure low thermal drift in the lens, an inbuilt temperature sensor adjusts the current value (0 to 290 mA) to maintain the focal length position. The tunable lenses offer a large transmission over the wavelength range of 240 to 2500 nm and a polarization-maintaining capability which is a straightforward addition to the beam manipulation system. Since all microscope objective lenses have a fixed focal length, it is possible that any axial shift of focus could lead to beam distortion. Figure 2(cviii) shows a single cross-section of the beam. However, to assess the beam intensity along the focus, a sequence of cross sections for different currents of the tunable lens is captured and characterised.

Figure 3(a) shows the beam measurement setup, while (b) and (c) show the intensity distribution of a diverging vortex beam in an axial plane for applied current $I_c = 0$ and 8 mA, respectively. The chosen optical vortex beam has a topological charge of $l = 2$ which exhibit a larger divergence of the beam. This meant that the trapped particles will be located within the field of view of the orthogonal microscopy imaging platform for characterizing the dynamics of the particle. The power of the beam at the focus is equal to 0.18W, approximately 20% of the direct output power out of the laser. In the diverging region, the beam size increases gradually with z , and the peak intensity decreases rapidly: from 2.4×10^9 W/m² in the focal plane $z = 0$ to 6.84×10^6 W/m² at $z = 1$ mm away from the focus.

The dependence of the diameter of central dark spot is plotted in Fig. 3(d), where the diameter is determined by the distance between the intensity peaks. The divergence angle, defined as the full angle of the dark cone of the beam, is ~ 0.0386 rad. When a current is applied to the tunable lens, the focal length of the lens changes, which moves the focus of the diverging vortex beam, as shown in Fig. 3(d). The radius r_l of a vortex beam with topological

charge $l = 2$ changes as $r_{l=2} = w_0 \left(1 + z^2 \lambda^2 / \pi^2 w_0^4\right)$, here z is the distance from the focal plane, λ is the laser wavelength, and w_0 is the $1/e^2$ beam waist, $w_0 = \lambda / (\pi NA) = 5.1 \mu\text{m}$. When the current increases from 0 to 16 mA, the focus moves linearly toward $-z$ direction by distance of $-14 \mu\text{m}$ per mA as shown in Fig. 3(e). As the movement of the focus is small comparing to the focal length the objective (2.1 mm), the beam profiles and its waist at different currents has a small change in addition to the relative shift. For example, when the input current is equal to 8 mA, the waist is $4.9 \mu\text{m}$, and the diverging angle increases to 0.0433 rad.

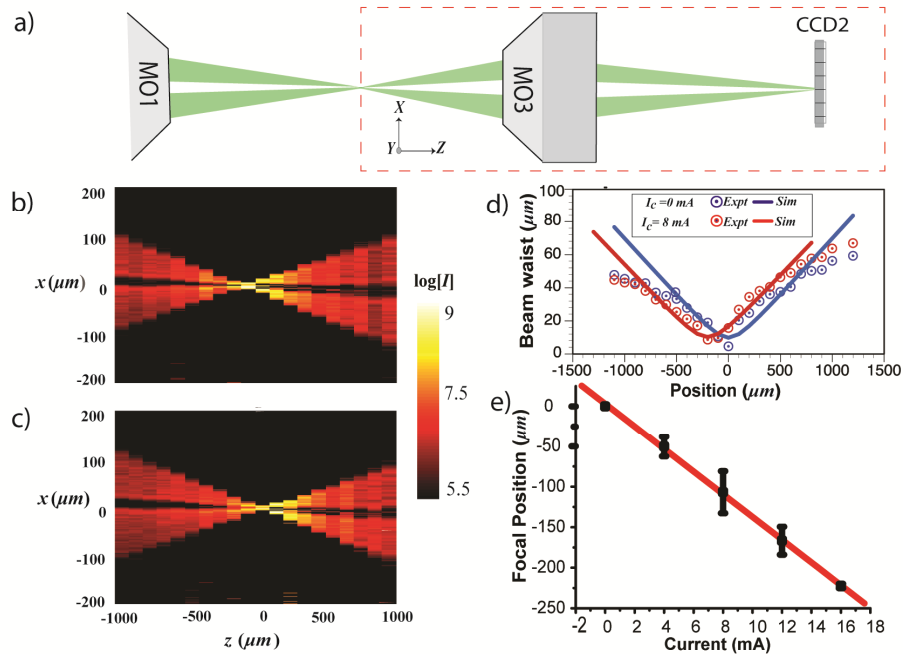


Fig. 3. Measurement of intensity distribution of diverging optical vortex beam ($l = 2$). a) shows the setup used to capture the transverse (xy) intensity profile of the beam over different z distance. b) and c) shows the intensity distribution in xz plane for applied current $I_c = 0$ mA and 8 mA. The beam waist at the two focus position is plotted in (d). (e) shows the focal position with varying current input into the tunable lens.

3. Results

Light-absorbing particles were dropped from the top into the glass cuvette and trapped at an equilibrium axial position where the gravitational downward force and the photophoretic upward force are counterbalanced. The stability of trapping in the transverse direction was ensured by the symmetry in the intensity of the doughnut-shaped vortex beam. The movement of the trapped particles was monitored by a fast camera, whose frame rate is 300 Hz for a full view 640×480 pixels (4.736×3.552 mm). The particle positions were tracked in real time by a centre-of-mass algorithm following the imaged shadow. In the following section 3.1-3.3, we present the measured dynamics of particles for different current modulations, namely sinusoidal and rectangular. Graphite-coated glass microspheres were chosen in our experiment due to their high absorption index. The diameter of the spheres ranges from 2 to $12 \mu\text{m}$.

3.1. Step-wise movements

The single levitated (balancing of forces, Fig. 4(a)) particle was then manipulated by controlling the tunable lens. Figure 5 shows the motion of a stable trapped $9.5 \mu\text{m}$ diameter

particle over a distance of 100 μm . The particle is trapped at 325.3 μm (average) above the focus for zero current. The applied current increases from 0 to 10 mA at a step size of 2 mA that reflect a stepwise change (0.1s) in the trapping position of average position stability of 0.98 μm as shown in Fig. 4(b). Whilst there is some discrepancy in particle step size, the particle position has almost a linear change with respect to the applied current of around 18.3 $\mu\text{m}/\text{mA}$ as shown in Fig. 4(c) (red line).

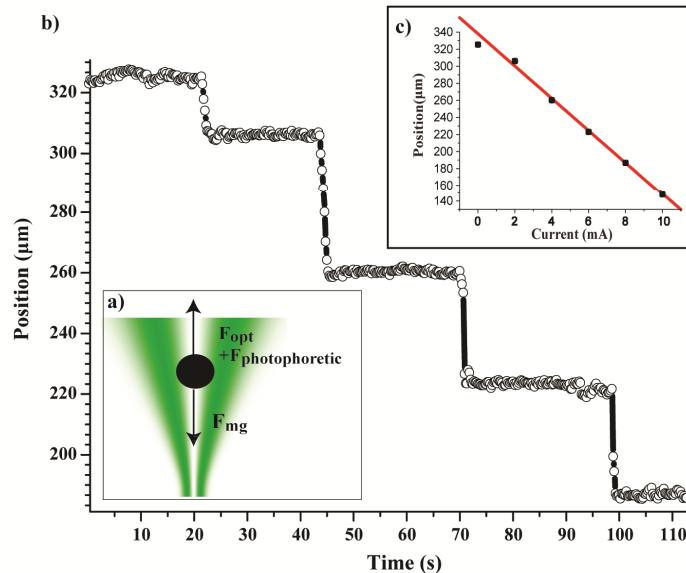


Fig. 4. a) Illustrate controlled optical manipulation of a graphite particle by balancing mass of particle with optical pressure and photophoretic forces. b) Traces of particle position trapped and shifted incrementally with tunable lenses (error bar, standard deviation $\sim 1 \mu\text{m}$). c) Linear dependence (red line) of the current with measured particle position (black square).

3.2. Oscillating movements

Next, we oscillate the beam with sinusoidal and rectangular modulations at a fixed frequency to demonstrate the level of control over the optically trapped particle. In both curves, a trapped particle motion closely follows the current change. A rectangular current signal with frequency is set at 0.2 Hz with amplitude ranging from 0 to 6 mA. The particle tracks are shown in Fig. 5 (blue line). The expected change in focus position is plotted (red) against the particle position (blue) which oscillates between 225 μm and 350 μm periodically. The rate of change of beam (focus) position is governed by the response time of the tunable lens (\sim few milliseconds). However, the particle lags behind due to the drag force in air. Based on results shown in Fig. 5, it takes 0.83s for the particle to get to equilibrium position from high (350 μm) to low (225 μm) positions; while it takes 0.63s to move from low to high positions. This is due to fact that the drag force always acts in the direction opposite to the movement of the particle, whereas gravity always acts in the downward direction. This effect becomes more obvious with the rectangular repetition curves where there is a sudden change of the focus position. Overall, the repeated delivery of particle over a distance of 100 μm has been clearly demonstrated. Next we move onto the measurement of drag force by measuring the escape velocity.

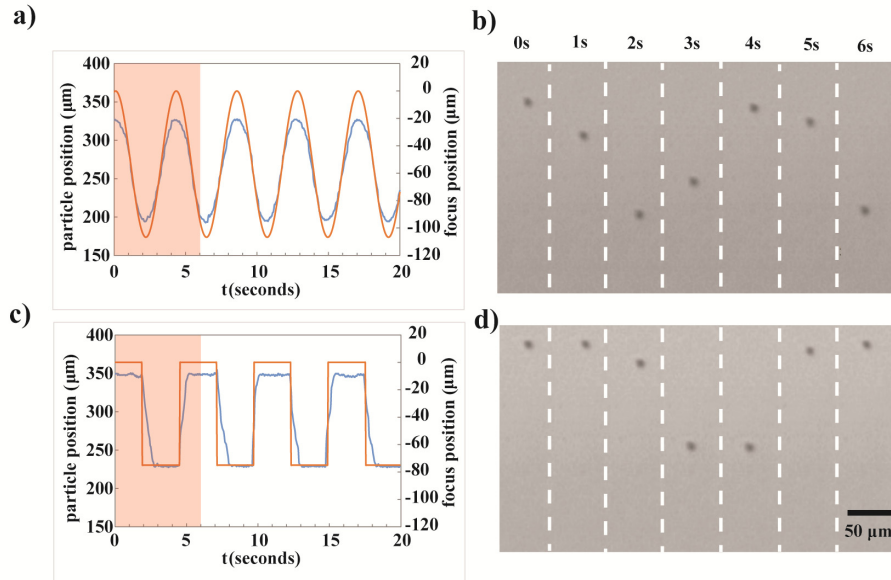


Fig. 5. Particle dynamic (a) The sinusoidal current signal with frequency ~ 0.2 Hz changes the beam focus position periodically (red line), which oscillates the particle on the beam axis sinusoidally (blue line). (b) Extract frames of the recorded particle motion corresponding to pink shaded area in (a) (Visualization 1). (c) – The rectangular current signal with frequency ~ 0.2 Hz changes the beam focus position (red line), which periodically changes the particle position on the beam axis from $225 \mu\text{m}$ to $350 \mu\text{m}$ from the focal plane (blue line). (d) Extract frames of the recorded particle motion corresponding to a single oscillating period (pink shaded area in c) (Visualization 2).

3.3. Drag force

Figure 5(c) shows the presence of drag forces imposed on the particle when the equilibrium trapping position was rapidly changing, i.e. when the beam is modulated with a rectangular repetitive curve. In order to measure the drag force, a free-fall particle is required as illustrated in Fig. 6(a), which was achieved with an amplitude modulation of the beam using a chopper inserted into the optical path. When the light beam is blocked by the chopper, the particle enters into free-fall (terminal velocity), Fig. 6(ai). When the light beam is unblocked, the particle is propelled upwards with an opposing drag force, Fig. 6(aii), before reaching the trapping equilibrium in Fig. 6(ciii). At this point, the drag force F_d ($6\pi\eta rv$) balances the gravity force F_{mg} (mg), where m is the mass of the particle, g is the acceleration of gravity, $\eta_{air} = 18.3 \mu\text{Pa}\cdot\text{s}$ is the viscosity of air at atmospheric pressure, r is radius of the particle and v is its velocity. When the beam is unblocked, the particle moves up to the equilibrium position as the photophoretic force F_{pp} counters both drag and gravity forces and levitates at the equilibrium position. A particle is trapped stably at $386 \mu\text{m}$ by the diverging vortex beam with power of 0.148 W . The particle will drop down when the laser beam is blocked with a constant speed as the upward directed drag force is counterbalanced by gravity. Taking the measured escape/terminal velocity of $\sim 0.1028 \text{ cm/s}$ (obtained from the linear fit, Fig. 6(b) dotted red line) and the measured particle size imaged in CCD1 of $5 \pm 1 \mu\text{m}$. By taking the density of graphite as 2.2 g/cm^3 and particle size to be $5 \mu\text{m}$ in diameter, the calculated drag force is $F_{drag} = 1.77 \pm 0.03 \times 10^{-12} \text{ N}$ and thus the mass of the trapped graphite particle is $1.77 \pm 0.03 \times 10^{-10} \text{ g}$. The obtained value of photophoretic force correlates well with the theoretically predicted force ($1.88 \times 10^{-12} \text{ N}$) [12] imposed on the particle by the levitating vortex beam.

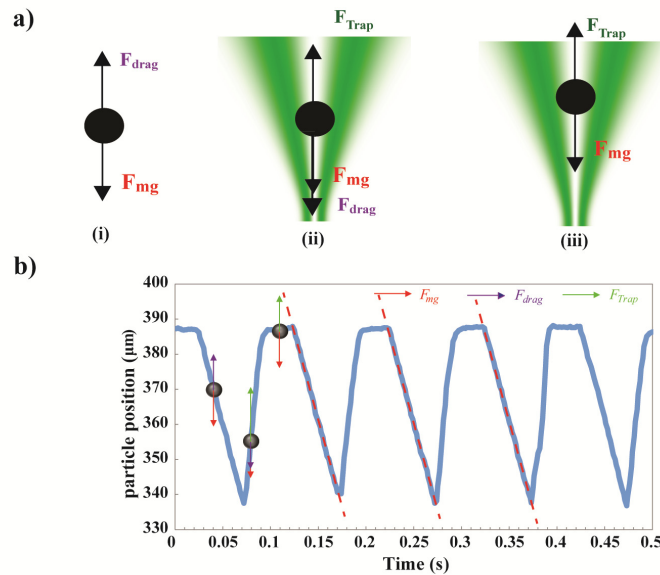


Fig. 6. (a) Forces acting on the particle without trap (i), with trapping beam ‘on’ for a particle moving to equilibrium position (ii) and at the equilibrium position. The chopper modulates the intensity (on-off) at frequency of 10 Hz. (b) shows the experimental result of the particle position under the same condition in Fig. 6(a). A linear fit (least square) is plotted to estimate the velocity of the particle.

4. Conclusions

In conclusion, we demonstrated the time-controlled manipulation of airborne particles using an electrical tunable lens and spatial light modulator. In addition, the methods described here provide a methodology for removing aberrations in the beam using a single mode fibre. The trapping particle dynamics showed that particles are stably trapped ($\pm 0.9 \mu\text{m}$) over a range of $100 \mu\text{m}$ with pico-Newton forces. The measured photophoretic force correlates to within $\sim 6\%$ of the theoretically predicted forces. The controlled manipulation allows the precise measurement of the mass of a single particle with a response time of 100 ms. The presented studies lay a foundation for application of focus-tunable electrical lenses for touch-less precise positioning of bioparticles at the focal spot of an x-ray free electron laser synchronised with the arrival of the x-ray pulse. This should significantly enhance the efficiency of delivery of particles to X-ray focus of XFEL for studies of nanoscale morphology of proteins and viruses in femtosecond coherent diffractive imaging experiments. The combination of a free-space particle manipulation tool with analytical characterisation [17] opens up the possibilities of in situ measurements of properties of aerosol particles in natural environments, where a small number of particles can be accurately delivered and positioned in a measurement (imaging or spectroscopy) system, that is of critical importance in many fields ranging from aerosol toxicology to climate science. Hence, it is plausible that the delivery of aerosolized particles, viruses and biological macromolecules through laser-induced photophoretic forces can improve the efficiency of delivery process. In addition, an all optical delivery approach could remove any unnecessary background scatter which is present in liquid injection techniques

Acknowledgements

We are grateful for valuable comments from Richard Kirian.. This work has been supported by the Australian Research Council under DP110100975. W. M. Lee acknowledges the support of Australian Research Council Early Career Researcher Award, DE160100843.